

# Simulations of Wind Field Effect on Two-Stream Waves in the Equatorial Electrojet

Chi-Lon Fern<sup>1,\*</sup> and Fu-Shong Kuo<sup>2</sup>

<sup>1</sup> General Education Center, National Yunlin University of Science and Technology, Douliou, Yunlin, Taiwan, ROC

<sup>2</sup> Department of Electro-Optical Engineering, Van Nung University, Chung-Li, Taiwan, ROC

Received 20 July 2007, accepted 31 March 2008

## ABSTRACT

The wind field effect on the phase velocities of 3- to 10-meter Farley-Buneman two-stream waves in the equatorial E region ionosphere at altitudes in the range of 95 - 110 km is studied by numerical simulation. The behavior of this two-stream wave in the uniform wind field  $U_n$  in a plane perpendicular to the Earth's magnetic field is simulated with a two-dimensional two-fluid code in which electron inertia is neglected while ion inertia is retained. It is confirmed that, the threshold condition for the appearance of two-stream waves is  $V_D^{th} = (1 - \sin^2 \theta)^{1/2} C_s / \cos \theta + U_n$ ; and the phase velocity of the two-stream wave at the threshold condition is  $V_p = C_s + U_n \cos \theta$ , where  $\theta$  is the elevation angle of the wave propagation in a limited range and  $\theta = \tan^{-1} (v_{in} / v_{ie})$ . The first formula indicates that the wind field parallel (anti-parallel) to the electron drift velocity will raise (lower) the threshold drift velocity by the amount of the wind speed. This means that parallel wind is a stable factor, while anti-parallel wind is an unstable factor of two-stream waves. This may explain why high speed (larger than acoustic speed) two-stream waves were rarely observed, since larger threshold drift velocity demands larger polarization electric field. The result of the simulations at the saturation stage show that when  $V_D$  was only slightly larger than  $V_D^{th}$ , the horizontal phase velocity of the two-stream wave would gradually down-shift to the threshold phase velocity  $C_s + U_n$ . The physical implications of which are discussed.

Key words: Two-stream wave, Wind field, E-region, Equatorial electrojet

Citation: Fern, C. L. and F. S. Kuo, 2009: Simulations of wind field effect on two-stream waves in the equatorial electrojet. *Terr. Atmos. Ocean. Sci.*, 20, 395-409, doi: 10.3319/TAO.2008.03.31.01(AA)

## 1. INTRODUCTION

Chemical release measurements (Larsen and Odom 1997; Larsen et al. 1998, Larsen 2000, 2002) of neutral winds in the mesosphere and lower thermosphere have shown large winds in the 100 to 110-km altitude range with maximum speeds between 100 and 150 m s<sup>-1</sup>. A three-dimensional numerical model calculation (Hysell et al. 2002) indicated that large horizontal neutral winds have strong effects on the equatorial electro-jet and low latitude ionospheric current system. These reports suggest that routine neutral wind measurements are required to advance the research of the effects of neutral wind on the equatorial electro-jet, and a proper formula of wind effects is needed.

Balsley et al. (1976) attempted to estimate wind velocities from measuring the phase velocities of type 1/type 2 waves in the electro-jet. They assumed in their measurements that

the phase velocity of type 1 waves (two stream waves) in the frame of reference of ions was the ion acoustic velocity; hence, the Doppler velocity observed by radar on the ground would be

$$\vec{V}_p = \vec{C}_s + \vec{k} \cdot \vec{U}_n / k \quad (1)$$

where  $\vec{V}_p$  is the wave phase velocity;  $\vec{U}_n$  is the neutral wind velocity; and  $\vec{k}$  is the radar wave vector. Broche et al. (1978) also derived the phase velocities of type 1 and type 2 irregularities to illustrate the role of neutral winds, and obtained the same Eq. (1) at the threshold condition. Hanuise and Crochet (1981) applied Eq. (1) to reduce the phase velocities of 5 - 50-m wavelength type 1 waves from their radar observation data, and found that the phase velocity of short scale waves ( $\approx 5$  m) was near the nominal ion acoustic velocity (around 360 m s<sup>-1</sup>).

Another interesting explanation for the higher phase ve-

\* Corresponding author  
E-mail: fengcl@yuntech.edu.tw

licity of two-stream waves, besides the neutral wind effect, is the heating effect possibly resulting from large electron drift velocity (e.g., St.-Maurice et al. 1986; Robinson and Honary 1990; Jones et al. 1991; Ravindran and Reddy 1993; Chen et al. 1995; Nielsen et al. 2002) and electron thermal fluctuations (St.-Maurice and Choudhary 2003), namely, ion acoustic velocity will be raised by enhanced temperature due to heating effects. Therefore, the higher phase velocity of two-stream waves is excited at a new threshold velocity larger than the nominal ion acoustic velocity. Additionally, large phase velocity two-stream waves were seldom observed by radar in regions besides the equatorial and the auroral region (e.g., Schlegel and Haldoupis 1994; Huang and Chu 1998; Haldoupis et al. 2002). Voiculescu and Ignat (2005) showed theoretically that parallel wind hinders the generation of waves and anti-parallel wind reduces significantly the electric field strength required for exciting waves. Their idea provides a clue for studying wind field effects on two-stream waves, specifically the potential important role of the wind field effect on the threshold condition for the excitation two-stream waves. In this study, we will not only investigate the wind field effect on the threshold condition of Farley-Buneman instability by numerical simulations, but also study the wind field effect on the phase velocity of two-stream waves.

In the past, 2D simulation studies of two-stream waves under windless conditions (Oppenheim and Otani 1996; Fern et al. 2001) found that the waves propagate dominantly in the same direction of the electro-jet even in the saturation stage and phase velocity in a direction other than the electro-jet direction was found to travel at a speed larger than acoustic speed but smaller than the phase velocity predicted by linear theory. The existing nonlinear 2D simulations have not yet proven that the phase velocity of saturated two-stream waves equals ion acoustic velocity, but it is widely accepted that the saturated phase velocities of radar observations are closely related to the threshold phase velocity that can be obtained by our simulations and also other analysis of phase velocity. In this paper, a horizontal background wind field was incorporated in a two-dimensional simulation code for studying wind field effects on two-stream waves. We will present our simulation result, along with an equation for functional dependence of the phase velocity of type 1 waves on neutral wind in the linear stage. In addition, possible wind field effect on the threshold condition will also be investigated to study saturation phase velocity. From our simulation and analysis, implications of Eq. (1) can be further interpreted, and the wind field effect on the generation of two-stream waves is presented.

## 2. NUMERICAL MODEL AND METHOD OF DATA ANALYSIS

### 2.1 Numerical Model

Our numerical model is similar to that of the previous studies by Fern et al. (2001) except that a neutral wind field

is taken into consideration in this study. The  $x$ -axis of the rectangular coordinate system points to the east, the  $y$ -axis points to the north and the  $z$ -axis points upward. The set of equations that are solved is a subset of the full governing equations. They consist of the continuity equation of plasma:

$$\frac{\partial n}{\partial t} + \bar{\nabla} \cdot (n \bar{V}_e) = 0 \quad (2)$$

the electron and ion velocity equations:

$$\bar{v}_e = \frac{\left(\frac{\Omega_e}{v_{en}}\right)^2 \left[ \frac{\bar{E}'}{B_0} + \frac{K_B T_e}{e B_0} \frac{\bar{\nabla} n}{n} + \frac{v_{en}}{\Omega_e} (\bar{V}_D - \bar{U}_n) \right] \times \frac{\bar{B}_0}{B_0}}{1 + \left(\frac{\Omega_e}{v_{en}}\right)^2} - \frac{\frac{\Omega_e}{v_{en}} \left[ \frac{\bar{E}'}{B_0} + \frac{K_B T_e}{e B_0} \frac{\bar{\nabla} n}{n} + \frac{v_{en}}{\Omega_e} (\bar{V}_D - \bar{U}_n) \right]}{1 + \left(\frac{\Omega_e}{v_{en}}\right)^2} \quad (3)$$

$$\frac{\partial \bar{v}_i}{\partial t} = -\frac{K_B T_i}{m_i} \frac{\bar{\nabla} n}{n} + \Omega_i \left( \frac{\bar{E}' + \bar{E}_0}{B_0} + \bar{v}_i \times \frac{\bar{B}_0}{B_0} \right) - v_{in} (\bar{v}_i - \bar{U}_n) - (\bar{v}_i \cdot \bar{\nabla}) \bar{v}_i \quad (4)$$

and the equation for quasi-neutrality condition:

$$\bar{\nabla} \cdot \bar{J} = 0 \quad (5)$$

Where  $\bar{J} = ne(\bar{V}_i - \bar{V}_e) = ne(\bar{v}_i - \bar{V}_D - \bar{v}_e)$  is the current density and  $n$  is the number density of the plasma;  $K_B$  is the Boltzmann constant;  $v_{in}, v_{en}, \Omega_i, \Omega_e, T_i, T_e, \bar{B}_0, \bar{E}', \bar{U}_n, \bar{V}_D, \bar{v}_e, \bar{v}_i$  are the ion-neutral collision frequency, the electron-neutral collision frequency, ion gyro-frequency, electron gyro-frequency, ion temperature, electron temperature, magnetic field, perturbation electric field, neutral wind velocity, mean flow electron drift velocity, perturbation electron and ion velocity, respectively.  $\bar{V}_i$  and  $\bar{V}_e$  can be taken as  $\bar{V}_i = \bar{v}_i; \bar{V}_e = \bar{V}_D - \bar{v}_e$ . Substituting all these physical quantities into Eq. (5), we obtain Eq. (6):

$$\begin{aligned} & \nabla^2 \Phi + \frac{\partial \Phi}{\partial x} \left( \frac{\partial n / \partial x}{n} - \kappa_e \frac{\partial n / \partial z}{n} \right) + \frac{\partial \Phi}{\partial z} \left( \kappa_e \frac{\partial n / \partial x}{n} + \frac{\partial n / \partial z}{n} \right) \\ & = \frac{K_B T_e}{e} \left( \frac{\partial^2 n / \partial x^2}{n} + \frac{\partial^2 n / \partial z^2}{n} \right) - B_0 V_D \left( \kappa_e \frac{\partial n / \partial x}{n} + \frac{\partial n / \partial z}{n} \right) \\ & + \left( \frac{1}{\kappa_e} + \kappa_e \right) B_0 \left( \frac{\partial n / \partial x}{n} v_{ix} + \frac{\partial n / \partial z}{n} v_{iz} + \frac{\partial v_{ix}}{\partial x} + \frac{\partial v_{iz}}{\partial z} \right) \\ & - B_0 U_n \left[ \frac{1}{\kappa_e} \left( \frac{\partial n / \partial x}{n} \right) - \left( \frac{\partial n / \partial z}{n} \right) \right] - B_0 \left( \frac{1}{\kappa_e} \frac{\partial U_n}{\partial x} - \frac{\partial U_n}{\partial z} \right) \end{aligned} \quad (6)$$

where  $\phi(x, z)$  is the potential function for the perturbed electric field  $\vec{E}$ , i.e.,  $\vec{E} = -\nabla\phi$ ; and  $\kappa_e$  is the ratio of the electron gyro-frequency to the electro-neutral collision frequency  $q_e B_0 / M_e \nu_{en}$ . The last two terms in the right hand side of Eq. (6) represent the neutral wind field effect, and were not included in the previous studies (e.g., Newman and Ott 1981; Oppenheim and Otani 1996; Fern et al. 2001). Here we like to emphasize that recombination (a term of the form  $\alpha n^2$ ) is ignored in the continuity Eq. (2), and the negligence of the recombination effect is appropriate for short-scale (smaller than 10 m) plasma waves (Haldoupis et al. 2005).

The Eqs. (3) and (4) were derived respectively from the momentum Eq. (7) by neglecting the gravitational term, and setting the time derivative term of electron species equal to zero, but retaining the time derivative term of ion species:

$$\rho_j \frac{d\vec{V}_j}{dt} = -\vec{\nabla} p_j + \rho_j \vec{g} + \frac{q_j \rho_j}{M_j} (\vec{E} + \vec{V}_j \times \vec{B}) - \rho_j \nu_{jm} (\vec{V}_j - \vec{U}_n) \quad (7)$$

The subscript  $j$  stands for plasma species,  $\rho_j = nM_j$  is the mass density of species  $j$ ;  $M_j$  and  $q_j$  are the particle mass and charge respectively; and  $p_j$  is the pressure of species  $j$ .

The mean flow eastward drift velocity  $\vec{V}_D$  of the electrons is driven by a vertically downward zero order polarization electric field:  $\vec{E}_0 = -\vec{V}_D \times \vec{B}_0$ , where  $\vec{B}_0 = B_0 \hat{e}_y$  is a constant magnetic field  $B_0$  of 0.28 G pointing to the north. The ion-neutral collision frequency  $\nu_{in}$  and electron-neutral collision frequency  $\nu_{en}$  are assumed to be constant in our simulation range with  $\nu_{in} = 2.5 \times 10^3 \text{ s}^{-1}$  and  $\nu_{en} = 4.0 \times 10^4 \text{ s}^{-1}$ . The ion and electron temperatures are assumed to be 230 K. The background plasma can be regarded as uniform with number density of  $1.0 \times 10^{11} \text{ m}^{-3}$ . These background parameters are similar to that used in the past studies of equatorial electro-jet (e.g., Sudan et al. 1973; McDonald et al. 1974; Fern et al. 2001). Since the phase velocity of two-stream wave also depends on both  $\nu_{in}$  and  $\nu_{en}$ , we added four more sets of  $(\nu_{in}, \nu_{en})$  as listed in Table 2 in the simulations to examine the accuracy of our code.

The numerical computations were performed on a two-dimensional Cartesian mesh using 121  $\times$  121 points in the  $x$ - $z$  plane. Periodic boundary condition is imposed on both electron density  $n$  and electric potential  $\phi$  in the  $x$  and  $z$  direction. The lengths  $X$  (east-west) and  $Z$  (vertical) of the simulation box were assigned case by case to study the waves of different scales. Flux-corrected transport (FCT) technique (Boris and Book 1973; Zalesak 1979) has been applied to carry out the time integration of the continuity Eq. (2). A detailed discussion of the application of FCT technique to study ionospheric irregularities can be referenced in Chou and Kuo (1996). At  $t = 0$ , the electrons are set to move

uniformly at drift speed  $\vec{V}_D$ , and the ions assume a constant velocity:  $\vec{V}_{i0} = (\nu_{in} \vec{E}_0 / \nu_{in} B_0) = \vec{U}_n$ . Then a density perturbation with amplitude  $\delta n = n_0 \sin(\ell x)$  is superposed on the background density  $n_0$ , where  $\ell$  is the wave-number to be assigned. At each time step of computation, the electron velocity at each grid point is calculated from Eq. (3), and the ion velocity at each grid is obtained by solving the differential Eq. (4) using 2<sup>nd</sup> order Runge-Kutta scheme. These velocities and densities at each grid are substituted into Eq. (6) to solve for the electric potential  $\phi(x, z)$  using the successive-over-relaxation (SOR) technique. Then, the plasma density distribution  $n(x, z)$  at time  $t + \delta t$  is calculated by the FCT scheme to complete one cycle of the computation. In order to guarantee numerical accuracy, we set the absolute error limit in the potential solver as small as  $10^{-4}$ . The simulation is called to stop whenever the absolute error of any grid fails to converge to within this error limit within 10000 steps of SOR iteration. By taking very small time step size and a double-precision scheme, no artificial dissipation was needed to prevent numerical instability throughout the simulations in this study.

This code was well tested in a previous study (Fern et al. 2001) under the windless condition: The growth rate of two-stream wave obtained by simulations of the one-dimensional model, the phase velocity of two-stream wave, and the Farley-Buneman threshold obtained by simulations of the two-dimensional model were all found to be consistent with the prediction of the linear theory presented by Rogister and D'Angelo (1970). So we consider this code as a proper tool to investigate the neutral wind effect on two-stream wave propagation.

## 2.2 Method of Data Analysis

By a series of computations, the plasma density  $n(x, z, t)$  at each grid point at every time step is obtained. Then the spatial-Fourier analysis of plasma density variation in the  $x$ -direction at a fixed height  $z$  and at time  $t$  (we sampled only the first time step of every 100 steps without loss of wave information) is made to obtain the information of different wave modes:

$$n(x, z, t) = \sum_{\ell} \{ A_{\ell}(z, t) \cos(\ell x) + B_{\ell}(z, t) \sin(\ell x) \} \quad (8)$$

The horizontal wavelength with wave-number  $\ell$  is  $2\pi/\ell$ , which is well defined by the horizontal length  $X$  of our simulation box. For example, the wavelength of the 9<sup>th</sup> horizontal spatial Fourier mode is  $X/9$ , and so forth. Then the coefficient  $A_{\ell}(z, t)$  is plotted as a function of time  $t$  such as shown in Fig. 1, from which we estimate the wave period of each wave by measuring the time interval between two suc-

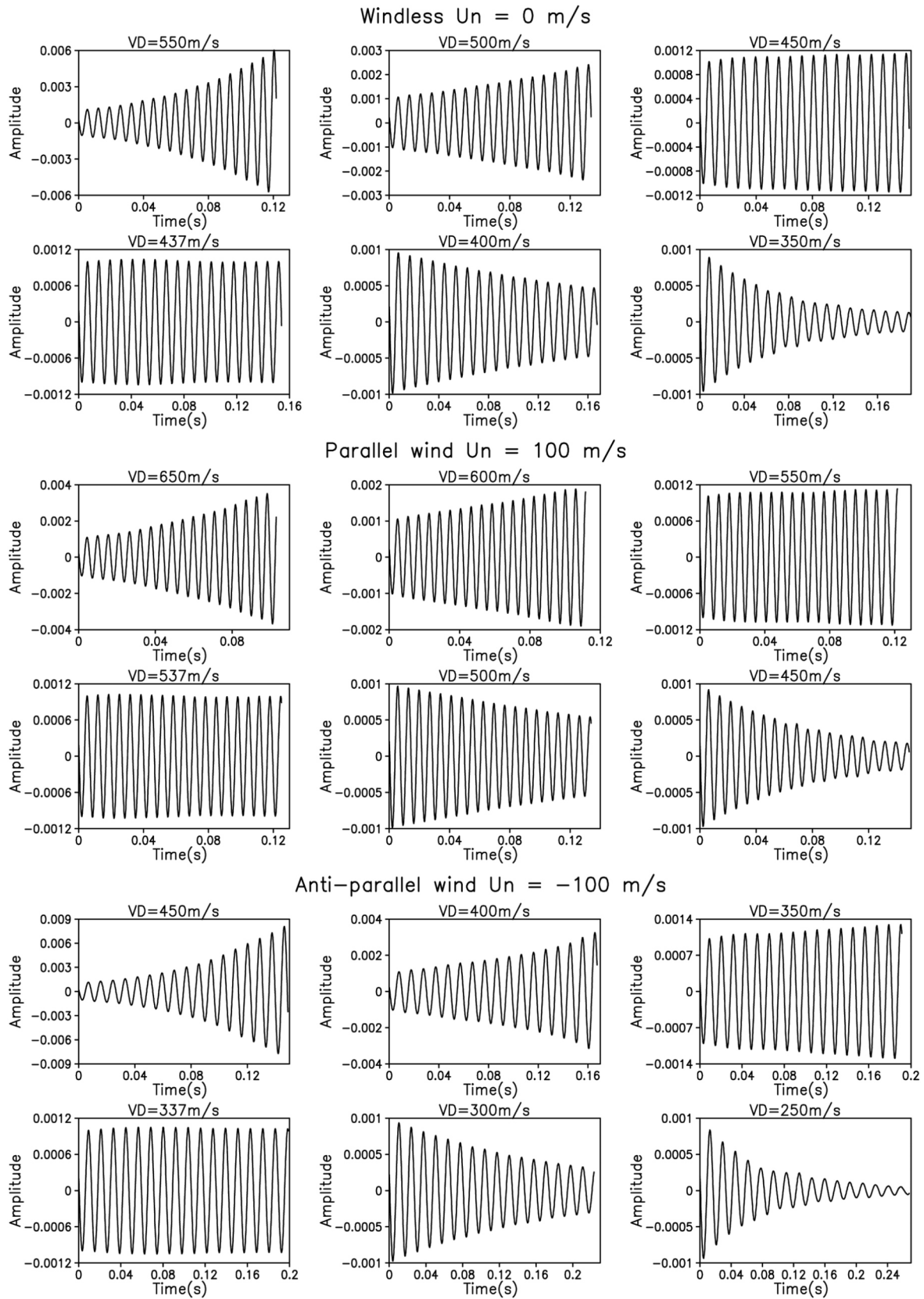


Fig. 1. Plots of the coefficient  $A(z, t)$  of  $\cos(kx)$  as a function of time  $t$  in the existence of various drift velocities for windless case ( $U_n = 0 \text{ m s}^{-1}$ ), parallel wind case ( $U_n = 100 \text{ m s}^{-1}$ ) and anti-parallel wind case ( $U_n = -100 \text{ m s}^{-1}$ ), where  $z$  is the 80<sup>th</sup> height and  $k = 0.209 \text{ m}^{-1}$  is the 9<sup>th</sup> horizontal Fourier mode (3-meter wave) in the X-Z simulation box with  $X = 27 \text{ m}$  and  $Z = 108 \text{ m}$ .

cessive peaks, hence the horizontal phase velocity can be determined. We also identify each wave from the plotting as a growing or dampening wave, since the wave will neither grow nor dampen at the threshold condition, we may estimate the Farley-Buneman threshold for the two-stream wave by a series of simulations at different electron drift- and wind velocities.

### 3. FORMULAS OF PHASE VELOCITY AND THE THRESHOLD CONDITION OF TWO-STREAM WAVES

The phase velocity of type 1 irregularities in the absence of neutral wind was given by (Fejer et al. 1975; Forbes 1981):

$$V_p^{(0)} = \hat{k} \cdot (\vec{V}_e + \Psi_0 \vec{V}_i) / (1 + \Psi_0) \quad (9)$$

where  $\hat{k} = \vec{k}/k$ , and  $\Psi_0 = v_{te}/v_{ti} = 0.23$ . And the threshold condition for the appearance of type-1 irregularities was given by

$$\hat{k} \cdot (\vec{V}_e - \vec{V}_i) = C_s (1 + \Psi_0) \quad (10)$$

Let's assume that Eqs. (9) and (10) are also valid when the neutral wind field exists, and the validity of this assumption can be examined by numerical simulation. Consider a two-stream wave with its wave vector  $\vec{k} = k(\vec{a}_x \cos \theta + \vec{a}_z \sin \theta)$  propagating in the uniform neutral wind  $\vec{U}_n = U_n \vec{a}_x$ , here  $\theta$  is the (radar beam elevation) angle between the vector  $\vec{k}$  and  $\vec{U}_n$ . The steady state equation of the ion velocity obtained by setting  $V_i/t = 0$  in Eq. (4) is:

$$\vec{V}_i = \vec{U}_n + \eta \frac{\vec{E}_0}{B_0} + \eta \vec{V}_i \times \frac{\vec{B}_0}{B_0} \quad (11)$$

where  $\eta = v_{te}/v_{in} = 0.036$ . In the two-dimensional model with  $\vec{B}_0 = B_0 \vec{a}_y$ ,  $\vec{E}_0 = E_0 \vec{a}_z$ , and  $\vec{V}_D = V_D \vec{a}_x = (E_0/B_0) \vec{a}_x$ , the solution  $\vec{V}_i$  of Eq. (11) is obtained as:

$$\vec{V}_i = V_{ix} \vec{a}_x + V_{iz} \vec{a}_z \quad (12)$$

where

$$V_{ix} = \frac{U_n + \eta^2 V_D}{1 + \eta^2} \cong U_n + \eta^2 V_D \quad (13a)$$

$$V_{iz} = \frac{\eta}{1 + \eta^2} (U_n - V_D) \cong \eta (U_n - V_D) \quad (13b)$$

Substituting  $\vec{V}_e = \vec{V}_D$  and Eqs. (13a), (13b) into Eqs. (9) and (10) and neglecting the higher (than 2<sup>nd</sup>) order terms of

$\eta$ , we obtain the horizontal phase velocity Eq. (14) and the threshold condition for the appearance of two-stream wave (type 1 wave) Eq. (15), respectively:

$$V_p^{(0)} = \left( \frac{\cos \theta - \Psi_0 \eta \sin \theta}{1 + \Psi_0} \right) V_D + \left( \frac{\Psi_0}{1 + \Psi_0} \right) (\cos \theta + \eta \sin \theta) U_n \quad (14)$$

$$V_D^{th} \cong \frac{C_s (1 + \Psi_0)}{\cos \theta + \eta \sin \theta} + U_n \quad (15)$$

At threshold condition, the phase velocity Eq. (14) becomes:

$$V_p^{(th)} = \left( \frac{\cos \theta - \Psi_0 \eta \sin \theta}{\cos \theta + \eta \sin \theta} \right) C_s + U_n \cos \theta \quad (16)$$

where  $\eta \sin \theta \ll \cos \theta$  holds for the elevation angle of radar observation in the range  $\theta < 60^\circ$  and  $\eta = 0.036$ , Eq. (16) becomes:

$$V_p^{(th)} = C_s + U_n \cos \theta \cong C_s + \vec{k} \cdot \vec{U}_n / k \quad (17)$$

which is equivalent to Eq. (1) for two-stream wave propagating in any direction (with  $\theta < 60^\circ$ ). In other words, Eq. (1) insists that the type 1 wave propagation velocity detected by radar in any direction (with  $\theta < 60^\circ$ ) is the propagation velocity at threshold condition, and we shall come back to discuss the physical implication of this equation. Equation (15) clearly indicates that the neutral wind field has strong effect on the threshold condition in any direction of wave propagation, namely, the parallel (anti-parallel) wind will raise (lower) the threshold drift velocity in accordance with the wind speed. Since  $\Psi_0 = 0.23$  is well below 1 and Eq. (14) is meaningful only for  $V_D = V_D^{th}$ , it is understandable from Eq. (14) that the wind field effect on the phase velocity is mainly through its effect on the threshold drift velocity [first term of Eq. (14)]. We shall examine Eqs. (14) and (15) for the horizontally propagating waves ( $\theta = 0^\circ$ ) by numerical simulations. In addition, the linear growth rate for horizontally propagating plasma waves in the equatorial E region was given by Eq. (18) (Fejer et al. 1975):

$$\Gamma(\text{growth rate}) \approx (1 + \Psi_0)^{-1} \left\{ \frac{\Psi_0}{V_i} \left[ \left( \frac{k(V_D - V_i)}{1 + \Psi_0} \right)^2 - k^2 C_s^2 \right] + \frac{v_i (V_D - V_i)}{L_N \Omega_i (1 + \Psi_0)} \right\} - 2\alpha N_e \quad (18)$$

where  $\alpha$  is the recombination coefficient;  $N_e$  is the mean electron density;  $L_N = N_e / N_e$ ; and the other symbols are the same as previously defined. The gradient drift term and the recombination term in Eq. (18) are negligible in this study because the background density is assumed to be uniform, and the recombination effect is ignored in the continuity Eq. (2); i.e.,  $\alpha = 0$ . So Eq. (18) reduces to Eq. (19):

$$\Gamma(\text{growth rate}) \approx (1 + \Psi_0)^{-1} \left\langle \frac{\Psi_0}{\nu_i} \left\{ \left[ \frac{k(V_D - V_i)}{1 + \Psi_0} \right]^2 - k^2 C_s^2 \right\} \right\rangle \quad (19)$$

It is proper to assume that the ion drift velocity  $\vec{V}_i$  is nearly equal to wind velocity  $\vec{U}_n$  then:

$$\Gamma(\text{growth rate}) \approx (1 + \Psi_0)^{-1} \left\langle \frac{\Psi_0}{\nu_i} \left\{ \left[ \frac{k(V_D - U_n)}{1 + \Psi_0} \right]^2 - k^2 C_s^2 \right\} \right\rangle \quad (20)$$

Equation (20) represents the linear theory of the threshold condition of pure two-stream waves, and our simulation on wind field effect will also be cross-examined with Eq. (20) as well.

## 4. NUMERICAL RESULTS

### 4.1 Threshold Condition for Two-Stream Waves

In order to examine the reliability of the two-stream wave simulation code with the existence of neutral wind field, we repeated the test of the windless case and made a comparison with the wind field case. Thus, the background neutral wind conditions of  $U_n = 0 \text{ m s}^{-1}$ ,  $U_n = 100 \text{ m s}^{-1}$  (parallel to electron drift velocity), and  $U_n = -100 \text{ m s}^{-1}$  (anti-parallel to electron drift velocity) were applied respectively in our simulation. A series of simulations on two-stream wave were made on a simulation box with  $X = Z = 27 \text{ } 108 \text{ m}$  and following preset parameters:  $\nu_{in} = 2.5 \text{ } 10^3 \text{ s}^{-1}$ ,  $\nu_{en} = 4.0 \text{ } 10^4 \text{ s}^{-1}$ ,  $\nu_i = 89.42 \text{ s}^{-1}$ ,  $\nu_e = 4.92 \text{ } 10^6 \text{ s}^{-1}$ , so  $\alpha = 0.2273$ . A density perturbation with horizontal wavelength of 3 meters and amplitude  $\delta n = n_0 \sin(kx)$  was superposed on the background density  $n_0$  to start the computation. Figure 1 shows the time evolutions of this perturbation wave at the 80<sup>th</sup> height ( $z = 72 \text{ m}$ ) in six cases with different drift velocities. The grey scale map of the density in the simulation box at the end of the 18<sup>th</sup> cycle of the windless case with electron drift velocity  $V_D = 500 \text{ m s}^{-1}$  is shown in Fig. 2, which clearly reveals that the density variation is dominant in the x-direction (jet-stream direction).

The temperature of ions and electrons was assumed to be  $230 \text{ K}$  throughout this study, leading to an ion acoustic ve-

locity  $C_s = \sqrt{K_B(T_i + T_e)/(M_i + M_e)} = 356 \text{ m s}^{-1}$ . Equation (15) yields the threshold condition for a horizontally propagating wave:  $V_D^{th} = 437 \text{ m s}^{-1} + U_n$ . Figure 1 clearly shows that the two-stream waves grow for the cases with  $V_D > V_D^{th}$  and dampen for the cases with  $V_D < V_D^{th}$ , the possible threshold drift velocities were found to be close to the prediction of Eq. (15):  $V_D^{th} = 437 \text{ m s}^{-1}$  for windless case,  $V_D^{th} = 537 \text{ m s}^{-1}$  for the case with parallel wind with  $U_n = 100 \text{ m s}^{-1}$ , and  $V_D^{th} = 337 \text{ m s}^{-1}$  for the case with anti-parallel wind with  $U_n = -100 \text{ m s}^{-1}$ . In addition, the oscillation period of each case in Fig. 1 can be precisely determined by measuring the peak-to-peak interval. We took the average of as many intervals as possible to minimize the random error in each measurement; therefore the phase velocity could be determined for each case with high precision. Table 1 shows the estimation of phase velocities associated to each case in Fig. 1. The result that, the phase velocity ( $V_p = 353.5 \text{ m s}^{-1}$ ) at threshold condition ( $V_D^{th} = 437 \text{ m s}^{-1}$ ) in the windless case is very close to ion acoustic speed ( $C_s = 356 \text{ m s}^{-1}$ ), is in

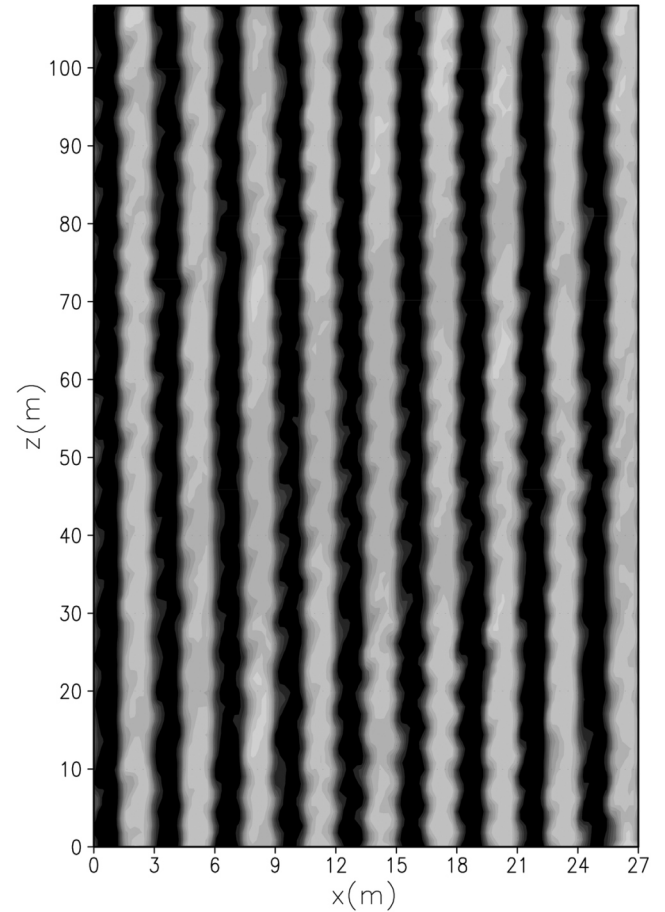


Fig. 2. A gray scale map of the density variation  $n(x, z)$  at  $t = 0.20 \text{ s}$  over the simulation box. The simulation started with a 3-meter wave perturbation; the dimension of the simulation box is  $27 \text{ } 108 \text{ m}$ , and the collision frequencies is CFS-1 (see Table 2), the neutral wind velocity is  $U_n = 0 \text{ m s}^{-1}$ , and the electron drift velocity is  $V_D = 500 \text{ m s}^{-1}$ .

Table 1. Horizontal phase velocities  $V_p(V_D)$  of 3-meter waves obtained by numerical simulations on a  $27 \times 108$  m simulation box in different electron drift velocities  $V_D$  for windless case ( $U_n = 0$  m s<sup>-1</sup>), parallel wind case ( $U_n = 100$  m s<sup>-1</sup>) and anti-parallel wind case ( $U_n = -100$  m s<sup>-1</sup>).

	$V_p(550)$	$V_p(500)$	$V_p(450)$	$V_p(437)$	$V_p(400)$	$V_p(350)$
$U_n = 0$ m s <sup>-1</sup>	443.31 m s <sup>-1</sup>	403.84 m s <sup>-1</sup>	364.04 m s <sup>-1</sup>	353.54 m s <sup>-1</sup>	323.59 m s <sup>-1</sup>	283.74 m s <sup>-1</sup>
	$V_p(650)$	$V_p(600)$	$V_p(550)$	$V_p(537)$	$V_p(500)$	$V_p(450)$
$U_n = 100$ m s <sup>-1</sup>	543.22 m s <sup>-1</sup>	503.57 m s <sup>-1</sup>	463.41 m s <sup>-1</sup>	452.83 m s <sup>-1</sup>	423.11 m s <sup>-1</sup>	382.63 m s <sup>-1</sup>
	$V_p(450)$	$V_p(400)$	$V_p(350)$	$V_p(337)$	$V_p(300)$	$V_p(250)$
$U_n = -100$ m s <sup>-1</sup>	344.64 m s <sup>-1</sup>	304.23 m s <sup>-1</sup>	264.65 m s <sup>-1</sup>	254.15 m s <sup>-1</sup>	224.64 m s <sup>-1</sup>	196.29 m s <sup>-1</sup>

agreement with the saturation velocity of radar observation. Based on the analysis of the windless case, it can be expected that the phase velocity at threshold condition corresponds to the phase velocity of radar observation. As shown in Table 1, the phase velocities at threshold in the eastward wind cases are also consistent with the prediction of Eq. (1) proposed by Balsley et al. (1976) for wind estimation of radar observation. It is obvious that the westward wind will lower the threshold by the amount of the wind speed for the eastward propagating wave while the eastward wind will do the opposite. But if we consider the same electron drift velocity, for example  $V_D = 450$  m s<sup>-1</sup> in Table 1, it can be seen that the wind field will cause the shift of phase velocity by only a fraction (20%) of the wind speed. Additionally, the estimated values of the linear growth rate (denoted by star in Fig. 3) by least square fitting are in agreement with the theoretical value predicted from Eq. (20) (denoted by solid curve in Fig. 3). Therefore, it is certain that the wind field does shift not only the phase velocity, but also the threshold value. A detailed proof of Eq. (14) relies on the simulations in the next section.

#### 4.2 Horizontal Phase Velocity with the Existence of Neutral Wind

Equation (14) indicates that the phase velocity is dependent on neutral wind  $U_n$  as well as the collision frequencies  $\nu_{in}$  and  $\nu_{en}$  through the parameter  $\theta = \nu_{in} \nu_{en} / \nu_{in} \nu_{en}$ . So we vary these parameters case by case while keeping the other parameters ( $\vec{B}_0, \vec{E}_0, T_e,$  and  $T_i$ ) unchanged, and set  $V_D = 500$  m s<sup>-1</sup>. The collision frequency sets (CFS) used in this study is listed in Table 2, and the neutral wind velocities were varied from -100 to 100 m s<sup>-1</sup>. Equations (14) and (15) also indicates that the phase velocity and the threshold drift velocity are independent of the wavelength in the absence of plasma density effect and kinetic effect, and we examined this property by analyzing two-stream waves of different wavelengths. So each case of simulation is identified by the neutral wind velocity, CFS and the scale lengths of its simulation box. The horizontal phase velocities predicted by Eq. (14) with  $\theta = 0$  at different cases are listed in Table 3 as a reference for comparison, and the corresponding results of simulations are summarized in Tables 4 and 5. Table 4 lists

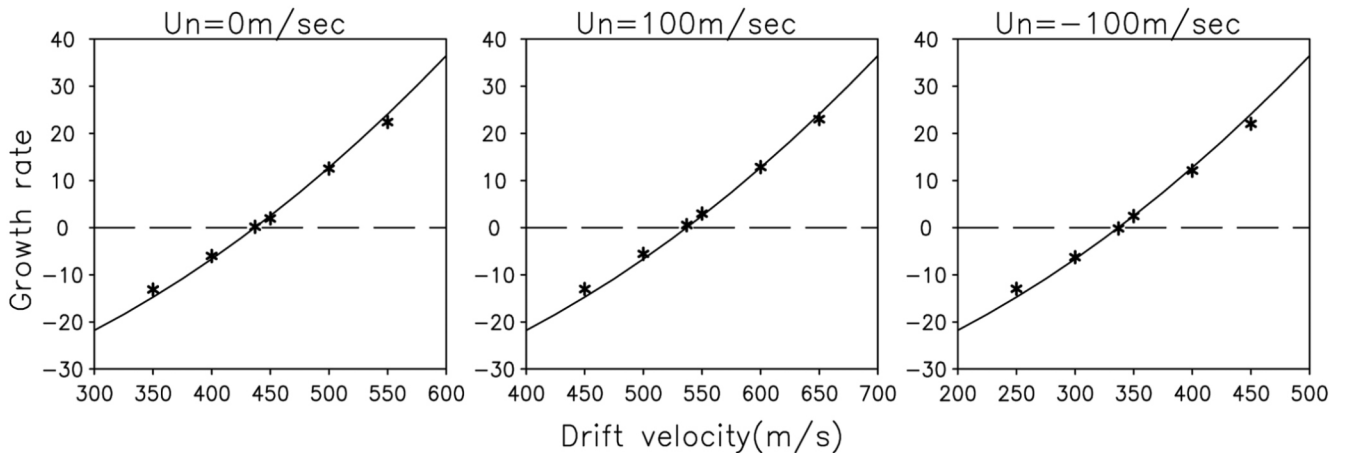


Fig. 3. Plots of the linear growth-rates of two-stream waves with respect to the electron drift velocity for windless case ( $U_n = 0$  m s<sup>-1</sup>), parallel wind case ( $U_n = 100$  m s<sup>-1</sup>) and anti-parallel wind case ( $U_n = -100$  m s<sup>-1</sup>), where the solid line represents the theoretical value obtained by Eq. (20), the asterisk represents the simulation results, and the dashed line represents the threshold value.

the phase velocities of the 10-m (horizontal wavelength) wave obtained by the simulations on a  $X \times Z = 90 \times 360$  m

simulation box; and Table 5 lists the phase velocities of the 3-m wave obtained by the simulations on a  $27 \times 108$  m box. By comparing the predicted phase velocities in Table 3 with the corresponding phase velocities resulting from simulations in Tables 4 and 5, we notice that most of the differences between them were smaller than 1%, and none exceeded 2%. This comparison proves that Eq. (14) is accurate, and the phase velocity of two-stream wave is independent of its wavelength. However, from the discussion in the previous section 4.1, it is believed that the Doppler velocities detected by radar were the phase velocity at threshold condition. Meanwhile, from Eq. (15), the variation of collision frequencies  $\nu_{in}$  and  $\nu_{en}$  which form the different parameter  $\Psi_0$  as listed in Table 2, can also cause variation of the threshold

Table 2. Collision frequency sets (CFS) in the numerical simulations.

	$\nu_{in}/s$	$\nu_{en}/s$	$\Psi_0$
CFS-1	$2.5 \times 10^3$	$4.0 \times 10^4$	0.2273
CFS-2	$3.0 \times 10^3$	$4.0 \times 10^4$	0.2728
CFS-3	$2.5 \times 10^3$	$4.8 \times 10^4$	0.2728
CFS-4	$2.5 \times 10^3$	$3.2 \times 10^4$	0.1818
CFS-5	$2.0 \times 10^3$	$4.0 \times 10^4$	0.1818

Table 3. Horizontal phase velocities  $V_p(U_n)$  with  $V_D = 500 \text{ m s}^{-1}$  in the existence of neutral wind  $U_n$  predicted by the Eq. (14) at  $\theta = 0^\circ$ ,

$V_p(U_n) = \frac{1}{1 + \Psi_0} \cdot V_D + \frac{\Psi_0}{1 + \Psi_0} \cdot U_n$  in 5 different collision frequency combinations. All velocities are in  $\text{m s}^{-1}$ .

	$V_p(100)$	$V_p(50)$	$V_p(0)$	$V_p(-50)$	$V_p(-100)$
CFS-1	425.91 $\text{m s}^{-1}$	416.66 $\text{m s}^{-1}$	407.40 $\text{m s}^{-1}$	398.14 $\text{m s}^{-1}$	388.88 $\text{m s}^{-1}$
CFS-2	414.26 $\text{m s}^{-1}$	403.55 $\text{m s}^{-1}$	392.83 $\text{m s}^{-1}$	382.12 $\text{m s}^{-1}$	371.40 $\text{m s}^{-1}$
CFS-3	414.26 $\text{m s}^{-1}$	403.55 $\text{m s}^{-1}$	392.83 $\text{m s}^{-1}$	382.12 $\text{m s}^{-1}$	371.40 $\text{m s}^{-1}$
CFS-4	438.46 $\text{m s}^{-1}$	430.77 $\text{m s}^{-1}$	423.08 $\text{m s}^{-1}$	415.39 $\text{m s}^{-1}$	407.70 $\text{m s}^{-1}$
CFS-5	438.46 $\text{m s}^{-1}$	430.77 $\text{m s}^{-1}$	423.08 $\text{m s}^{-1}$	415.39 $\text{m s}^{-1}$	407.70 $\text{m s}^{-1}$

Table 4. Horizontal phase velocities  $V_p(U_n)$  of 10-meter waves with  $V_D = 500 \text{ m s}^{-1}$ . The simulations were performed on a  $90 \times 360$  m simulation box in 5 different collision frequency combinations. All velocities are in  $\text{m s}^{-1}$ .

	$V_p(100)$	$V_p(50)$	$V_p(0)$	$V_p(-50)$	$V_p(-100)$
CFS-1	423.15 $\text{m s}^{-1}$	414.27 $\text{m s}^{-1}$	405.76 $\text{m s}^{-1}$	396.30 $\text{m s}^{-1}$	387.82 $\text{m s}^{-1}$
CFS-2	411.61 $\text{m s}^{-1}$	400.69 $\text{m s}^{-1}$	389.69 $\text{m s}^{-1}$	380.88 $\text{m s}^{-1}$	368.71 $\text{m s}^{-1}$
CFS-3	411.83 $\text{m s}^{-1}$	400.69 $\text{m s}^{-1}$	390.53 $\text{m s}^{-1}$	380.88 $\text{m s}^{-1}$	370.52 $\text{m s}^{-1}$
CFS-4	435.83 $\text{m s}^{-1}$	430.53 $\text{m s}^{-1}$	420.84 $\text{m s}^{-1}$	413.83 $\text{m s}^{-1}$	405.97 $\text{m s}^{-1}$
CFS-5	436.06 $\text{m s}^{-1}$	428.72 $\text{m s}^{-1}$	420.84 $\text{m s}^{-1}$	414.27 $\text{m s}^{-1}$	405.12 $\text{m s}^{-1}$

Table 5. Horizontal phase velocities  $V_p(U_n)$  of 3-meter waves with  $V_D = 500 \text{ m s}^{-1}$ . The simulations were performed on a  $27 \times 108$  m simulation box in 5 different collision frequency combinations. All velocities are in  $\text{m s}^{-1}$ .

	$V_p(100)$	$V_p(50)$	$V_p(0)$	$V_p(-50)$	$V_p(-100)$
CFS-1	423.15 $\text{m s}^{-1}$	413.60 $\text{m s}^{-1}$	403.84 $\text{m s}^{-1}$	393.72 $\text{m s}^{-1}$	385.14 $\text{m s}^{-1}$
CFS-2	411.26 $\text{m s}^{-1}$	400.69 $\text{m s}^{-1}$	389.90 $\text{m s}^{-1}$	379.15 $\text{m s}^{-1}$	367.31 $\text{m s}^{-1}$
CFS-3	411.61 $\text{m s}^{-1}$	400.69 $\text{m s}^{-1}$	389.28 $\text{m s}^{-1}$	377.97 $\text{m s}^{-1}$	367.51 $\text{m s}^{-1}$
CFS-4	435.36 $\text{m s}^{-1}$	427.59 $\text{m s}^{-1}$	419.69 $\text{m s}^{-1}$	410.08 $\text{m s}^{-1}$	402.47 $\text{m s}^{-1}$
CFS-5	435.59 $\text{m s}^{-1}$	427.15 $\text{m s}^{-1}$	419.24 $\text{m s}^{-1}$	410.52 $\text{m s}^{-1}$	402.35 $\text{m s}^{-1}$

value, so we will continue to examine the phase velocity at threshold for both windless and wind field cases. Considering the case of CFS-2 in Table 2, Fig. 4 displays the time evolution of the horizontal 3-m wave for different drift velocities corresponding to different driving electric fields. The threshold drift velocity  $V_D^{th}$ , yielding neither growing nor dampening, is about  $V_D^{th} = 450 \text{ m s}^{-1}$  for the windless case and  $V_D^{th} = 550 \text{ m s}^{-1}$  for the case with neutral wind  $U_n = 100 \text{ m s}^{-1}$ . From estimation by the peak-to-peak method, it is found that the phase velocity at threshold is about  $351 \text{ m s}^{-1}$  (close to ion acoustic velocity  $C_s = 356 \text{ m s}^{-1}$ ) for the windless case and  $450 \text{ m s}^{-1}$  (close to  $C_s + U_n$ ) for the case with neutral wind  $U_n = 100 \text{ m s}^{-1}$ , and their difference is also close to the wind speed  $U_n = 100 \text{ m s}^{-1}$ . Based on the analysis of phase velocity at threshold condition, we confirmed the predictions of Eqs. (15) and (16) that the variation of collision frequency

does change the threshold drift velocity  $V_D^{th}$ , but does not change the phase velocity  $V_p$  at threshold condition.

### 4.3 Simulations of Two-Stream Waves with Wind Field at the Saturation Stage

It was proposed that the phase velocity of radar observations, mostly at threshold condition, resulted from nonlinear saturation (e.g., Lee et al. 1974; Rogister and Jamin 1975; Sudan 1983a, b). Although the 2D simulations of nonlinear saturation in windless cases ( $U_n = 0$ ) had been carried out by Oppenheim and Otani (1996) and Fern et al. (2001), their saturation phase velocities were smaller than the linear results, but still larger than the ion acoustic velocity. Moreover, there is no saturation simulation associated with the situation of the existence of a wind field. In this section, we

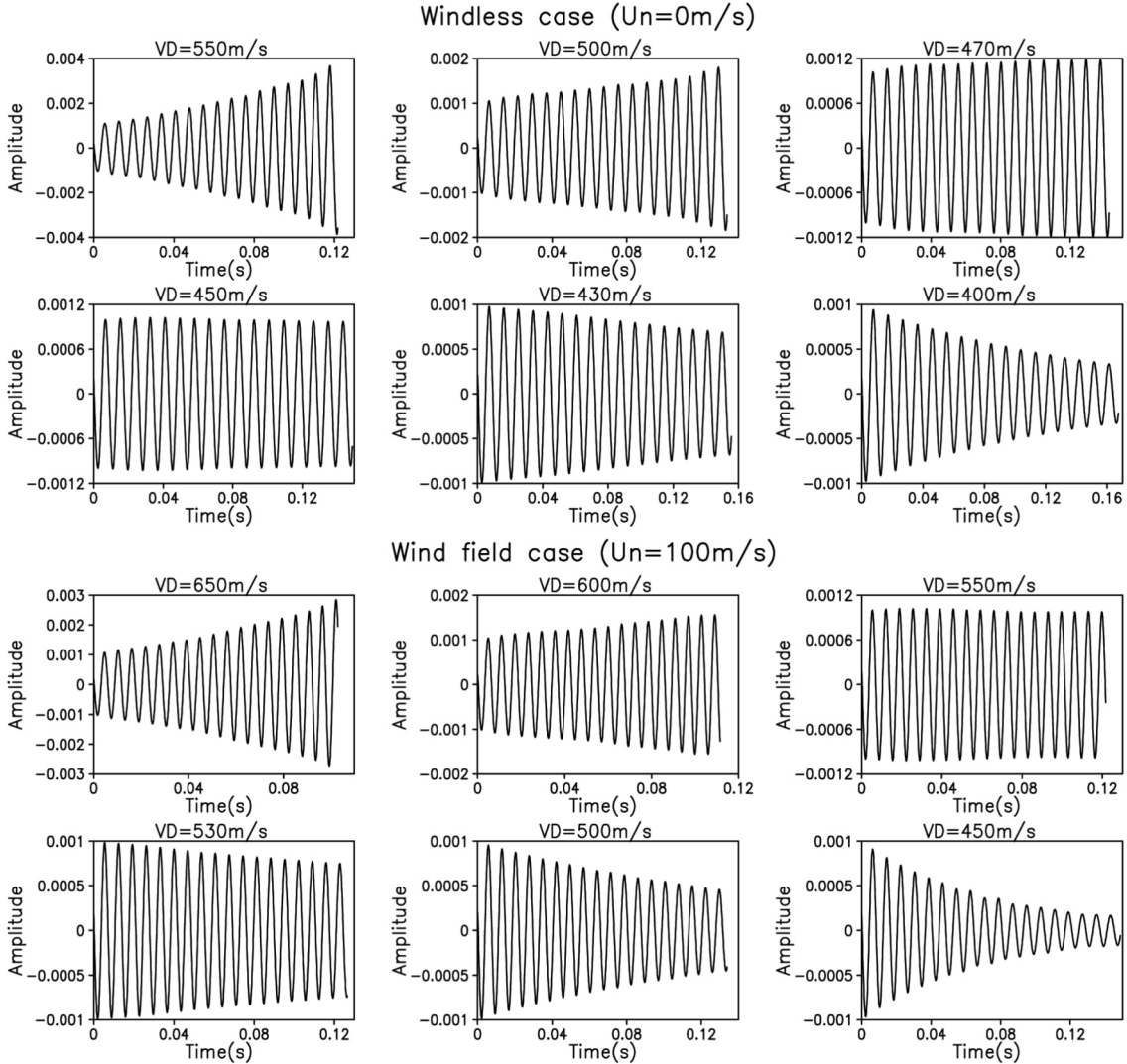


Fig. 4. Plots of the coefficient  $A(z, t)$  of  $\cos(kx)$  as a function of time  $t$  for various drift velocities in the windless case ( $U_n = 0 \text{ m s}^{-1}$ ) and wind field case ( $U_n = 100 \text{ m s}^{-1}$ ), where  $z$  is the 80<sup>th</sup> height and  $k = 2.09 \text{ m}^{-1}$  is the 9<sup>th</sup> horizontal Fourier mode (3-meter wave) in the  $X-Z$  simulation box with  $X = 27 \text{ m}$  and  $Z = 108 \text{ m}$  and the collision frequencies is CFS-2 (see Table 2).

will adopt electron drift velocity slightly larger than the threshold value to carry out the simulations of saturation by our two-fluid code. In fact, the past studies (e.g., St.-Maurice et al. 1986; Jones et al. 1991; Nielsen et al. 2002) indicated that, larger electron drift velocity would induce larger electron temperature, and consequently would raise the ion acoustic velocity. So it is reasonable to assume that the drift velocity should be near threshold value under the assumption of fixed temperature. In order to compare the phase velocity of a windless situation with that of the wind field situation, the simulations of two-stream wave for both situations were made on a simulation box with  $X = Z = 27 \times 108$  m and an initial density perturbation wave of 3 meters was introduced. The electron drift velocity  $V_D = 460$  m s<sup>-1</sup> (driving electric field  $E_0 = 12.88$  mV m<sup>-1</sup>) for the windless case and  $V_D = 560$  m s<sup>-1</sup> (driving electric field  $E_0 = 15.68$  mV m<sup>-1</sup>) for the case with neutral wind  $U_n = 100$  m s<sup>-1</sup> were considered. If the background parameters are the same as that in section 4.1, then according to Eqs. (15) and (16), the phase velocity  $V_p^{th}$  and electron drift velocity  $V_D^{th}$  at threshold condition corresponding to ion acoustic velocity of 356 m s<sup>-1</sup> should be  $V_p^{th} = 356$  m s<sup>-1</sup> and  $V_D^{th} = 437$  m s<sup>-1</sup> for the windless case. Similarly,  $V_p^{th} = 456$  m s<sup>-1</sup> and  $V_D^{th} = 537$  m s<sup>-1</sup> at threshold for the case with neutral wind  $U_n = 100$  m s<sup>-1</sup>.

Figure 5 shows the time evolutions of the standard deviation of the density for the case with  $U_n = 0$  m s<sup>-1</sup> (windless case) and the case with  $U_n = 100$  m s<sup>-1</sup> (wind field case). We can see from Fig. 5 that the simulations had extended to the saturation stage, where the primary wave stopped growing and the waves with different size and frequency were excited possibly from the nonlinear process. Therefore, the density variations in gray scale maps (see Fig. 6a) were much more randomized than that in Fig. 2. In order to make sure these density variations in Fig. 6a are not the result of numerical error (mostly truncation error), we rerun the simulations without initial wave perturbation. The results at exactly the same time stage (of Fig. 6a) were presented in Fig. 6b for comparison. The gray scale maps of density variations in Fig. 6b were very flat, meaning that the density variations in Fig. 6a were not the result of numerical error. It is better to analyze the horizontal phase velocity in the saturation stage by 2D Fourier analysis. Figure 7 shows the power spectra of phase velocity for a horizontal 3-m wave corresponding to the specific wave mode  $(k_x, k_z) = (9, 0)$ , where  $k_x$  represents horizontal mode, and  $k_z$  represents vertical mode. The location of the largest peak of power spectra in Fig. 7 allowed us to determine the phase velocity and the dominant oscillation frequency of the horizontal 3-m wave. For example, the power spectra plots (in the linear regime) of time interval  $t = 0.00 \sim 0.73$  s for the windless case and time interval  $t = 0.00 \sim 0.60$  s for the wind field case in the left panels of Fig. 7, reveal that the phase velocities of the largest peaks are close to the prediction of linear theory. Namely, the phase velocity evaluated from spectra power

is about 371 ~ 375 m s<sup>-1</sup> for the windless case and about 472 m s<sup>-1</sup> for the wind field case, and the phase velocities predicted by Eq. (14) of linear theory are 375 m s<sup>-1</sup> for the windless case and 475 m s<sup>-1</sup> for the wind field case. So, it is reliable to estimate the phase velocity from the location of the largest peak of power spectra. In the saturation regime, the power spectra plots in the time interval  $t = 2.18 \sim 2.91$  s for the windless case and time interval  $t = 2.39 \sim 2.99$  s for the wind field case, as shown in the right panels of Fig. 7 reveal that the phase velocities corresponding to the largest peaks were close to the threshold phase velocities: the phase velocity is about 358 m s<sup>-1</sup> for the windless case and 457 m s<sup>-1</sup> for the case with neutral wind  $U_n = 100$  m s<sup>-1</sup>. The spectral widths in the saturation stage are significantly larger than their respective counterparts in the linear regime. The above results are consistent with the characteristic of saturation spectra. We combined the linear spectra with the saturation spectra together in Fig. 8 by an expanded manner, we observed that the difference of their phase velocities is obvious and the phase velocities of saturation seemed to be limited in magnitude to threshold values. However, the threshold value of the wind field case is larger than the windless case. In other words, our result of simulations in the saturation stage shows that the neutral wind will shift the threshold drift velocity as well as the phase velocity. Due to the up-shift of threshold drift velocity, the excitation of two-stream waves needs a larger driving electric field, therefore the two-stream waves of larger phase velocity were not easily observed in the past radar observations.

#### 4.4 Saturation Phase Velocity of Various $(k_x, k_z)$ Modes

Figure 9 shows the phase velocity spectra of a few  $(k_x, k_z)$  modes in the first quadrant ( $k_x > 0, k_z > 0$ ) and the fourth quadrant ( $k_x > 0, k_z < 0$ ) of the windless case obtained from the time series in the time interval 2.18 ~ 2.91 s. In order to be compatible with the  $\omega$  spectra presented in our previous paper (Fern et al. 2001), we reflect the spectra in the fourth quadrant into the second quadrant ( $k_x < 0, k_z > 0$ ). The labels across the top give the value of  $k_x$  for that column, while the labels on the left give the values of  $k_z$  for that row, where  $k_x$  and  $k_z$  are respectively the horizontal and the vertical wave number in m<sup>-1</sup>. The analysis procedure used to obtain these spectra is described in section 2.2 of our previous paper (Fern et al. 2001). The top number in the upper corner in each plot shows the reduction in that mode's maximum density perturbation with respect to the mode with the largest density perturbation found in the simulation in decibels. The bottom number in the upper corner shows the total power contained in the mode compared to the total power in the mode containing the most power in decibels. The phase velocity of the  $(k_x, k_z)$ -mode was calculated by conventional definition  $v_{ph} = \omega / \sqrt{k_x^2 + k_z^2}$ , and its corresponding wave-

length is  $\lambda = 2\pi / \sqrt{k_x^2 + k_z^2}$ . The wavelengths of different  $(k_x, k_z)$ -modes are different. All the  $(k_x, k_z)$ -modes in Fig. 9 except the primary mode ( $k_x = 2.09, k_z = 0$ ) are believed to be of secondary waves arising from nonlinear processes.

We notice from Eq. (15) that the two-stream wave cannot be excited in a direction with an elevation angle  $\theta = \tan^{-1}(k_z/k_x) > 18.2^\circ$  by the electro-jet with  $V_D = 460 \text{ m s}^{-1}$  and  $U_n = 0 \text{ m s}^{-1}$ , but Fig. 9 reveals that waves propagate with phase speed  $C_s$  in a direction with an elevation angle

significantly larger than  $18.2^\circ$ . For example, when the elevation angle of the wave mode with  $k_x = 1.40$  and  $k_z = 0.87$  is  $31.9^\circ$ , the spectrum of this mode has a peak at  $C_s$ . These waves might be produced by some nonlinear processes since they were not excited by FB instability. Figure 9 also reveals that the phase velocity decreases from  $C_s$  to 0 as the elevation angle increasing from  $32^\circ$  to  $90^\circ$  (the spectra with  $k_x = 0$  have peak phase speed at 0 and a large spectral width, they are not shown in Fig. 9).

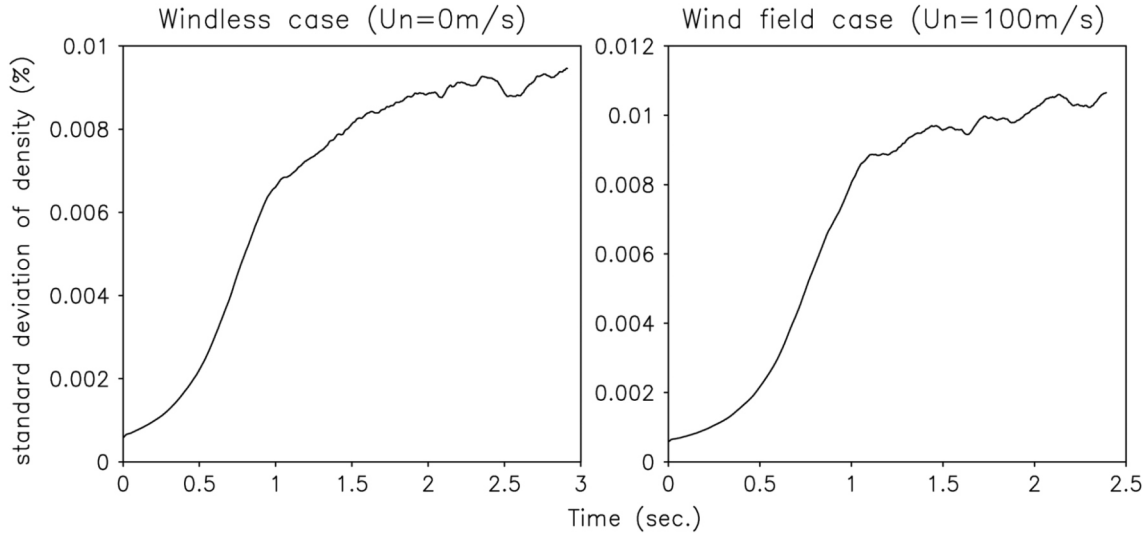


Fig. 5. The time evolution of the standard deviation of the spatial variation of density perturbation,  $\langle |\delta_n / n_0|^2 \rangle$ , for (left) windless case ( $U_n = 0 \text{ m s}^{-1}$ ) with  $V_D = 460 \text{ m s}^{-1}$  and (right) wind field case ( $U_n = 100 \text{ m s}^{-1}$ ) with  $V_D = 560 \text{ m s}^{-1}$ .

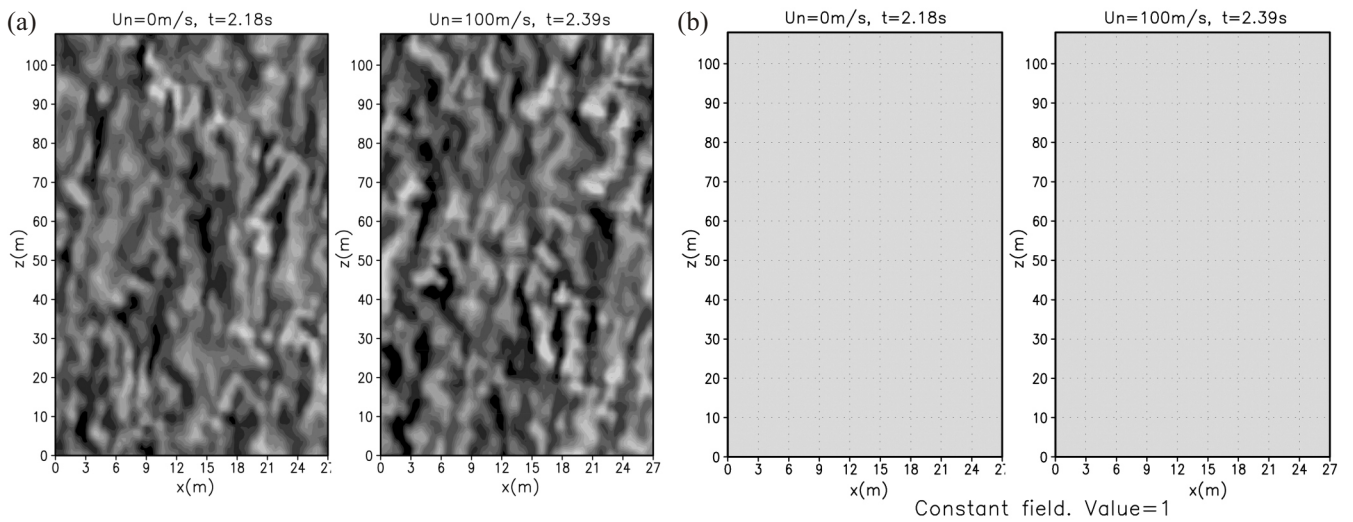


Fig. 6. (a) A gray scale map of the density variation  $n(x, z)$  at the saturation stage over the simulation box. Left panel: windless case ( $U_n = 0 \text{ m s}^{-1}$ ) with  $V_D = 460 \text{ m s}^{-1}$ ; Right panel: wind field case ( $U_n = 100 \text{ m s}^{-1}$ ) with  $V_D = 560 \text{ m s}^{-1}$ . The simulation started with a 3-meter wave perturbation. The dimension of the simulation box is  $27 \times 108 \text{ m}$ , and the collision frequencies is CFS-1 (see Table 2). (b) A gray scale map of the density variation  $n(x, z)$  at the same time stage of Fig. 6a over the simulation box. Left panel: windless case ( $U_n = 0 \text{ m s}^{-1}$ ) with  $V_D = 460 \text{ m s}^{-1}$ ; Right panel: wind field case ( $U_n = 100 \text{ m s}^{-1}$ ) with  $V_D = 560 \text{ m s}^{-1}$ . The simulation conditions were identical to that of Fig. 6a except that these simulations started with no initial wave perturbation. The density fluctuations were still flat after a long time of simulations, meaning that the numerical error did not grow to a point to confuse the physics of Fig. 6a.

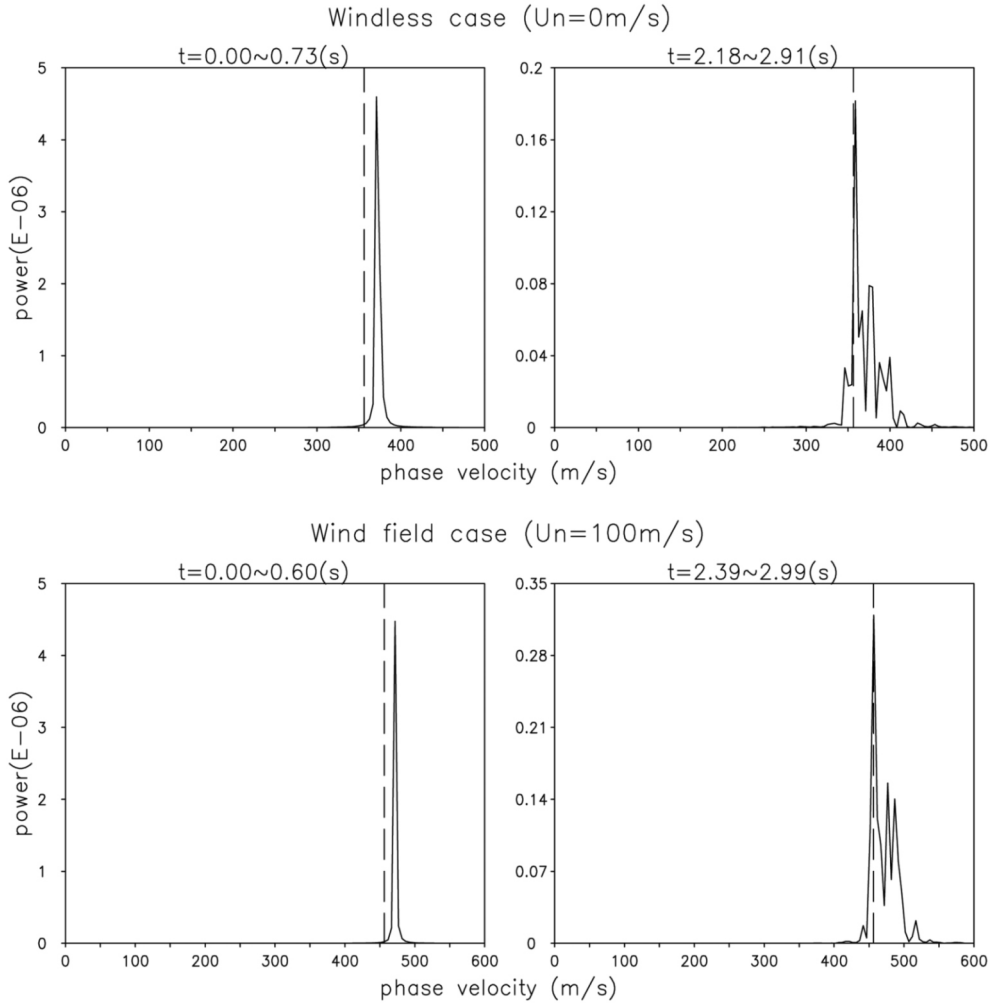


Fig. 7. Power spectra of windless case and wind field case generated from the density perturbation. The horizontal axis shows the phase velocity,  $v_{ph} = \omega / \sqrt{k_x^2 + k_z^2}$ , and the vertical axis shows the power of linear scale unit. The dashed line represents the phase velocity at threshold condition ( $C_s + U_n$ ), where  $356 \text{ m s}^{-1}$  for windless case and  $456 \text{ m s}^{-1}$  for wind field case. The electron drift velocity is  $V_D = 460 \text{ m s}^{-1}$  for windless case and  $V_D = 560 \text{ m s}^{-1}$  for the case with  $U_n = 100 \text{ m s}^{-1}$ .

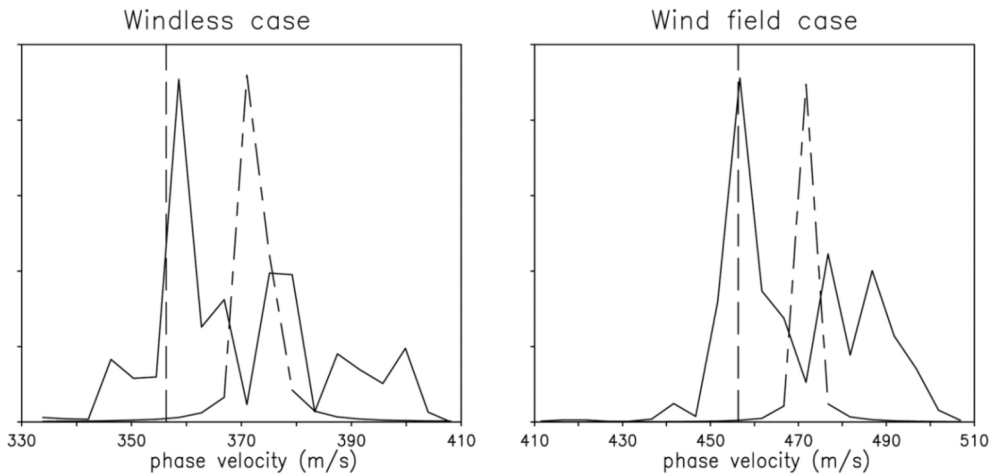


Fig. 8. The comparison of power spectra between linear regime and saturation regime for windless case and wind field case, where long-short dashed line represents the spectra of linear regime, and the solid line represents the spectra of saturation regime. The horizontal axis shows the phase velocity,  $v_{ph} = \omega / \sqrt{k_x^2 + k_z^2}$ , and the vertical axis shows the power with linear scale in arbitrary units.

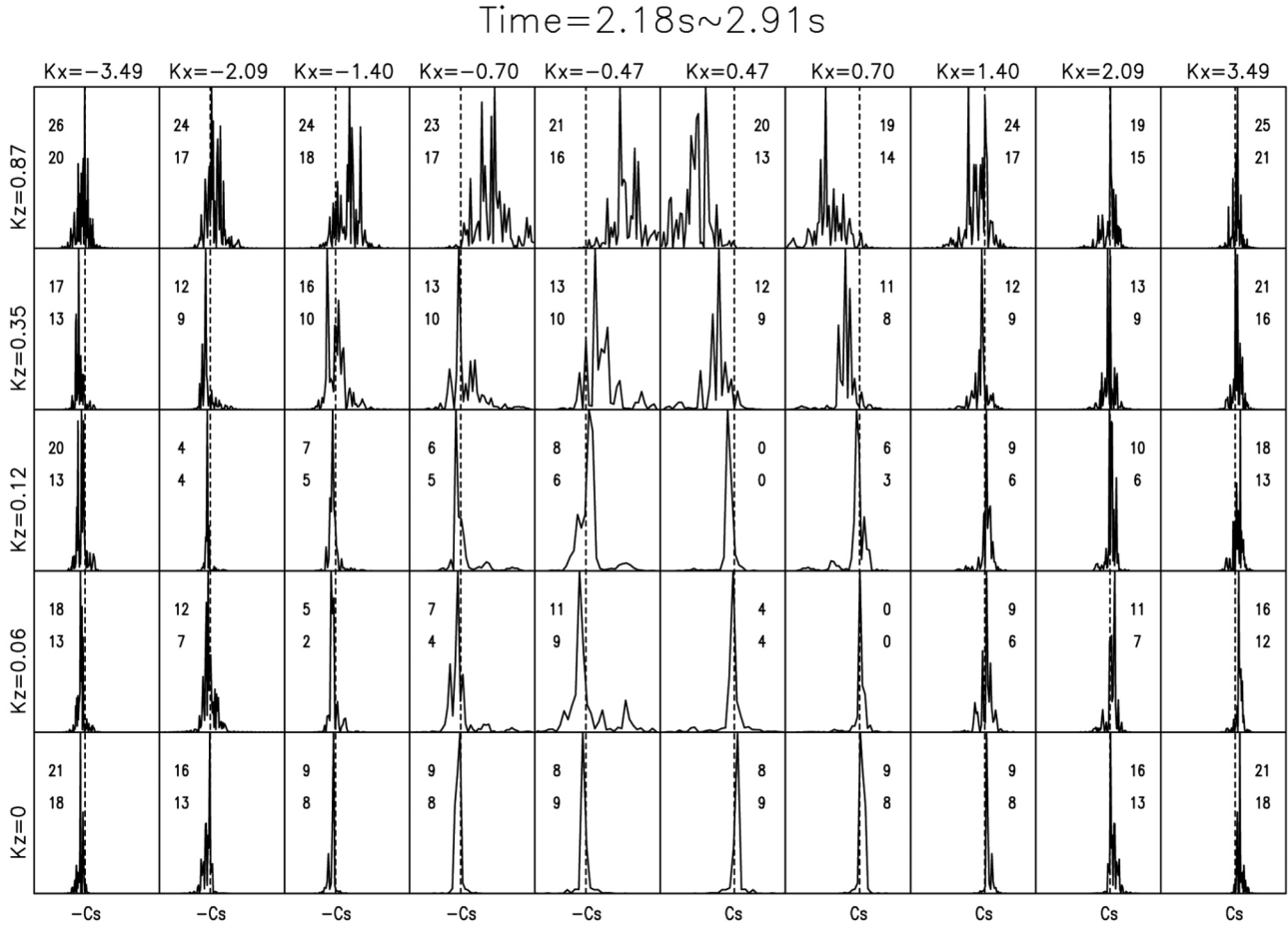


Fig. 9. The power spectra at saturation stage obtained from the windless case of Fig. 7 ( $V_D = 460 \text{ m s}^{-1}$ ,  $U_n = 0 \text{ m s}^{-1}$ ). The horizontal axis shows the phase velocity,  $v_{ph} = \omega / \sqrt{k_x^2 + k_z^2}$ , in unit of the sound speed  $C_s = 356 \text{ m s}^{-1}$ , while the vertical axis shows the power on a linear scale in arbitrary units. The label across the top give  $k_x$  (in  $\text{m}^{-1}$ ) for that column, while the labels on the left give  $k_z$  (in  $\text{m}^{-1}$ ) for that row. The top number in the upper corner of each plot shows the reduction in that mode's maximum density perturbation with respect to the mode with the largest density perturbation found in the simulation in decibels. The bottom number in the upper corner shows the total power contained in the mode compared to the total power of the mode containing the most power in decibels.

## 5. SUMMARY AND DISCUSSION

We have conducted 2D simulations of wind field effect on two-stream wave extending from the linear regime to the saturation regime. In the meantime, we have provided Eq. (14) to describe the phase velocity of two-stream wave in contrast to that of the conventional formula, Eq. (1). The two major controlling factors in Eq. (14) are electron drift velocity  $V_D$  and the neutral wind velocity  $U_n$ , while those in Eq. (1) are the ion acoustic velocity  $C_s$  and  $U_n$ . The direct neutral wind contribution to the phase velocity in the 2<sup>nd</sup> term of Eq. (14) ( $U_n \cos \theta$ ) is only a factor 0.2 of that in Eq. (1) ( $= U_n \cos \theta$ ), and the indirect contribution by neutral wind to the phase velocity in the 1<sup>st</sup> term of Eq. (14) is through its effect on the threshold condition as indicated by Eq. (15). These two formulas, Eqs. (1) and (14), are equivalent only at the threshold condition ( $V_D = V_D^{th}$ ) [see Eq. (16)]. Equation (1) was proposed for the purpose of wind measurement based on two assumptions: One was that all the type 1 waves ob-

served by radar were excited at the threshold condition, and the other one was that waves propagate at the ion acoustic velocity (in the reference frame of ions) no matter the angle to the current (Balsley et al. 1976; Broche et al. 1978). However, our numerical simulations have shown that the shift in threshold is roughly consistent with the prediction of Eq. (15). That is, the threshold value will be up-shifted when the wind field is parallel to the electron drift velocity, and conversely, the threshold will be down-shifted when wind field is anti-parallel to the electron drift velocity. Moreover, past observations and model calculations of neutral wind in the equatorial E region (e.g., Reddy and Devasia 1981; Larsen and Odom 1997; Hysell et al. 2002) indicate that the horizontal wind field is mostly parallel to the direction of drift velocity. If threshold drift velocity is not up-shifted by parallel neutral wind, and remains the same at near the ion acoustic velocity, then two-stream

waves with large phase velocity should be frequently observed due to the frequent appearance of parallel neutral wind. However, there are few radar observation data of large phase velocity two-stream waves in the E-region. This fact tends to support the up-shifted (by parallel wind) threshold value, which requires a large driving electric field, causing difficulty in the excitation of two-stream waves.

According to Eq. (18), the excitation of two-stream waves mainly depends on the difference between electron drift velocity and ion drift velocity  $\vec{V}_e - \vec{V}_i$ . Since ion drift velocity tends to move together with neutral wind due to the collision between the heavy ions and neutral atmospheric particles, neutral wind will change the velocity difference  $\vec{V}_e - \vec{V}_i$ . Consequently, electron drift velocity must also change to keep the difference  $\vec{V}_e - \vec{V}_i$  above the threshold condition. The growth rate as a function of the electron drift velocity for three different neutral wind velocities is presented in Fig. 3, from which the threshold electron drift velocity  $V_D^{th}$  can be determined, and the phase velocity at threshold can be evaluated by the peak-to-peak method. The threshold values determined by our simulations were in agreement with the prediction of Eq. (15). Also, when electron drift velocity is larger than the threshold, phase velocities at the linear stage are identical with the prediction of Eq. (14), which was derived in section 3. From the linear relation between electron drift velocity and phase velocity in the windless case ( $U_n = 0$ ), it can be expected that the phase velocity will be larger than ion acoustic velocity when the electron drift speed is larger than the threshold value. Therefore, the shift of phase velocity derived from the wind field is smaller when considering the same electron drift velocity for the windless and wind field cases. Although most of the radar observations did not yield a linear relation, it was found that large electron drift velocity or other wave dynamics will enhance plasma temperature (e.g., St.-Maurice et al. 1986; Jones et al. 1991; Ravindran and Reddy 1993; Nielsen et al. 2002; St.-Manurice and Choudhary 2003) raising ion acoustic velocity and consequently requiring a larger threshold velocity to excite two-stream waves. In this context, perhaps the small wind effect evaluated in Eq. (14) can be considered.

Of course, it is very difficult to construct a perfect model matching the complex circumstances of radar observations. Past simulation results (Oppenheim and Otani 1996; Fern et al. 2001) show that type 1 waves in the saturation stage travel dominantly in the same direction as the electro-jet at a phase velocity predicted by linear theory. In addition, phase velocity in a direction other than the electro-jet direction is found to be larger than acoustic speed but smaller than the phase velocity predicted by linear theory. Such results are due to the fact that the electron drift velocity assumed in their simulations is so much larger than the threshold value that their phase velocity cannot downshift to approach the ion acoustic velocity. In this study, we consider simulations of horizontal electron drift velocity slightly above the threshold

value and analyze horizontal primary waves. The results of our simulations reveal a clear difference between the phase velocities at the linear stage and at the saturation stage. The saturation phase velocity in the windless case is found to be close to the ion acoustic velocity  $C_s$ , and the horizontal saturation phase velocity in the wind field case is shifted to the phase velocity at threshold  $C_s + U_n$  as indicated by Eq. (17). Linear theory [namely, Eq. (14)] insists that two-stream waves can be excited by the electro-jet only within a small elevation angle (let's call it the threshold angle) when the electron drift velocity  $V_D$  is only slightly above a certain threshold value. The result of our simulation in the saturation stage (Fig. 9) shows that many waves propagated with phase speed  $C_s$  (for windless case) in the direction with an elevation angle significantly larger than this threshold angle. We believe that these secondary waves result from nonlinear processes and Eq. (1) is valid in a limited range of elevation angle in the forward direction of the electro-jet.

**Acknowledgements** This work is supported in part by National Science Council of Taiwan through the projects NSC 95-2111-M-224-001 and NSC 94-2111-M-238-001.

## REFERENCES

- Balsley, B. B., B. G. Fejer, and D. T. Farley, 1976: Radar measurements of neutral winds and temperatures in the equatorial E region. *J. Geophys. Res.*, **81**, 1457-1459, doi: 10.1029/JA081i007p01457. [[Link](#)]
- Boris, J. P. and D. L. Book, 1973: Flux-corrected transport, 1, SHASTA, A fluid transport algorithm that works. *J. Comput. Phys.*, **11**, 38-69, doi: 10.1016/0021-9991(73)90147-2. [[Link](#)]
- Broche, P., M. Crochet, and J. Gagnepain, 1978: Neutral winds and phase velocity of the instabilities in the equatorial electrojet. *J. Geophys. Res.*, **83**, 1145-1146, doi: 10.1029/JA083iA03p01145. [[Link](#)]
- Chen, P. R., L. Yi, and E. Nielsen, 1995: Variations of the mean phase velocity of 1-m ionosphere plasma waves with the plasma electron temperature. *J. Geophys. Res.*, **100**, 1647-1652. [[Link](#)]
- Chou, S. Y. and F. S. Kuo, 1996: A numerical study of the wind field effect on the growth and observability of equatorial spread F. *J. Geophys. Res.*, **101**, A8, 17137-17149, doi: 10.1029/96JA01404. [[Link](#)]
- Fejer, B. G., D. T. Farley, B. B. Balsley, and R. F. Woodman, 1975: Vertical structure of the VHF backscattering region in the equatorial electrojet and the gradient drift instability. *J. Geophys. Res.*, **80**, 1313-1324, doi: 10.1029/JA080i010p01313. [[Link](#)]
- Fern, C. L., S. Y. Chou, and F. S. Kuo, 2001: Simulations of spectral asymmetries of pure two-stream waves in the equatorial electrojet. *Chin. J. Phys.*, **39**, 141-162.
- Forbes, J. M., 1981: The equatorial electrojet. *Rev. Geophys.*, **19**, 469-504, doi: 10.1029/RG019i003p00469. [[Link](#)]

- Haldoupis, C., K. Schlegel, G. C. Hussey, and J. A. Koehler, 2002: Radar observation of kinetic effects at meter scales for Farley-Buneman plasma waves. *J. Geophys. Res.*, **107**, 1272, doi: 10.1029/2001JA009193. [[Link](#)]
- Hanuise, C. and M. Crochet, 1981: 5-50-m wavelength plasma instabilities in the equatorial electrojet 2. Two-stream conditions. *J. Geophys. Res.*, **86**, 3567-3572, doi: 10.1029/JA086iA05p03567. [[Link](#)]
- Huang, C. M. and Y. H. Chu, 1998: First observations of type 1 sporadic E irregularities in the equatorial anomaly region using the Chung-Li radar. *Geophys. Res. Lett.*, **25**, 3779-3782, doi: 10.1029/1998GL900024. [[Link](#)]
- Hysell, D. L., J. L. Chau, and C. G. Fesen, 2002: Effects of large horizontal winds on the equatorial electrojet. *J. Geophys. Res.*, **107**, 1214, doi: 10.1029/2001JA000217. [[Link](#)]
- Jones, B., P. J. S. Williams, K. Schlegel, T. Robinson, and I. Haggstrom, 1991: Interpretation of enhanced electron temperatures measured in the auroral E-region during ERRRIS campaign. *Ann. Geophys.*, **9**, 55-59.
- Larsen, M. F., 2000: Coqui 2: Mesospheric and lower thermospheric wind observations over Puerto Rico. *Geophys. Res. Lett.*, **27**, 445-448, doi: 10.1029/1999GL010704. [[Link](#)]
- Larsen, M. F., 2002: Winds and shears in the mesosphere and lower thermosphere: Results from four decades of chemical release wind measurements. *J. Geophys. Res.*, **107**, 1215, doi: 10.1029/2001JA000218. [[Link](#)]
- Larsen, M. F. and C. D. Odom, 1997: Observations of altitudinal and latitudinal E-region neutral wind gradients near sunset at the magnetic equator. *Geophys. Res. Lett.*, **24**, 1711-1714, doi: 10.1029/97GL01469. [[Link](#)]
- Larsen, M. F., S. Fukao, M. Yamamoto, R. Tsunoda, K. Igarashi, and T. Ono, 1998: The SEEK chemical release experiment: Observed neutral wind profile in a region of sporadic E. *Geophys. Res. Lett.*, **25**, 1789-1792, doi: 10.1029/98GL00986. [[Link](#)]
- Lee, K., C. F. Kennel, and F. V. Coroniti, 1974: On the marginally stable saturation spectrum of unstable type I equatorial electrojet irregularities. *J. Geophys. Res.*, **79**, 249-266, doi: 10.1029/JA079i001p00249. [[Link](#)]
- McDonald, B. E., T. P. Coffey, S. Ossakow, and R. N. Sudan, 1974: Preliminary report of numerical simulation of type 2 irregularities in the equatorial electrojet. *J. Geophys. Res.*, **79**, 2551-2554, doi: 10.1029/JA079i016p02551. [[Link](#)]
- Newman, A. L. and E. Ott, 1981: Nonlinear simulations of type I irregularities in the equatorial electrojet. *J. Geophys. Res.*, **86**, 6879-6891, doi: 10.1029/JA086iA08p06879. [[Link](#)]
- Nielsen, E., C. F. del Pozo, and P. J. S. Williams, 2002: VHF coherent radar signals from the E region ionosphere and the relationship to electron drift velocity and ion acoustic velocity. *J. Geophys. Res.*, **107**, 1012, doi: 10.1029/2001JA900111. [[Link](#)]
- Oppenheim, M. and N. Otani, 1996: Spectral characteristics of the Farley-Buneman instability: Simulation vs. observation. *J. Geophys. Res.*, **101**, 24573-24582, doi: 10.1029/96JA02237. [[Link](#)]
- Ravindran, S. and C. A. Reddy, 1993: Variation of type I plasma wave phase velocity with electron drift velocity in the equatorial electrojet. *J. Geophys. Res.*, **98**, 21581-21591, doi: 10.1029/93JA01051. [[Link](#)]
- Reddy, C. A. and C. V. Devasia, 1981: Height and latitude of electric fields and currents due to local east-west winds in the equatorial electrojet. *J. Geophys. Res.*, **86**, 5751-5767, doi: 10.1029/JA086iA07p05751. [[Link](#)]
- Robinson, T. R. and F. Honary, 1990: A resonance broadening kinetic theory of the modified two-stream instability: Implications for radar auroral backscatter experiments. *J. Geophys. Res.*, **95**, 1073-1085, doi: 10.1029/JA095iA02p01073. [[Link](#)]
- Rogister, A. and N. D'Angelo, 1970: Type 2 irregularities in the equatorial electrojet. *J. Geophys. Res.*, **75**, 3879-3887, doi: 10.1029/JA075i019p03879. [[Link](#)]
- Rogister, A. and E. Jamin, 1975: Two-dimensional nonlinear processes associated with 'Type 1' irregularities in the equatorial electrojet. *J. Geophys. Res.*, **80**, 1820-1828, doi: 10.1029/JA080i013p01820. [[Link](#)]
- Schlegel, K. and C. Haldoupis, 1994: Observation of the modified two-stream plasma instability in the midlatitude E region ionosphere. *J. Geophys. Res.*, **99**, 6219-6226, doi: 10.1029/93JA02869. [[Link](#)]
- St.-Manurice, J. P. and R. K. Choudhary, 2003: Fast type-I waves in the equatorial electrojet: Evidence for nonisothermal ion-acoustic speeds in the lower E region. *J. Geophys. Res.*, **108**, 1170, doi: 10.1029/2002JA009648. [[Link](#)]
- St.-Manurice, J. P., C. Hanuise, and E. Kudeki, 1986: On the dependence of the phase velocity of equatorial irregularities on the polarization electric field and theoretical implications. *J. Geophys. Res.*, **91**, 13493-13505, doi: 10.1029/JA091iA12p13493. [[Link](#)]
- Sudan, R. N., 1983a: Unified theory of type I and type II irregularities in the equatorial implications. *J. Geophys. Res.*, **88**, 4853-4860, doi: 10.1029/JA088iA06p04853. [[Link](#)]
- Sudan, R. N., 1983b: Nonlinear theory of type I irregularities in the equatorial electrojet. *Geophys. Res. Lett.*, **10**, 983 pp.
- Sudan, R. N., J. Akinrimisi, and D. T. Farley, 1973: Generation of small-scale irregularities in the equatorial electrojet. *J. Geophys. Res.*, **78**, 240-248, doi: 10.1029/JA078i001p00240. [[Link](#)]
- Voiculescu, M. and M. Ignat, 2005: Wind effect on the plasma instabilities operating in the midlatitude ionospheric E region. *Romanian Reports in Physics*, **57**, 953-970.
- Zalesak, S. T., 1979: Fully multidimensional flux-corrected transport algorithms to fluids. *J. Comput. Phys.*, **31**, 335-362, doi: 10.1016/0021-9991(79)90051-2. [[Link](#)]